Available online at www.sciencedirect.com
SCIENCE DIRECT
Journal of Sound and Vibration 293 (2006) 587–598
JOURNAL OF SOUND AND VIBRATION
www.elsevier.com/locate/jsvi

An analytical model for ground vibrations from accelerating trains

Anders Karlström*

Department of Applied Mechanics, Chalmers University of Technology, SE-412 96 Göteborg, Sweden

Accepted 26 August 2005
Available online 18 January 2006

Abstract

An analytical approach is used to investigate ground vibrations due to accelerating and decelerating trains. The ground is modelled as a stratified half-space with linearly viscoelastic layers. On top of the ground, a rectangular embankment is placed, supporting the rails and the sleepers. The rails are modelled as Euler–Bernoulli beams where the propagating forces (wheel loads) are acting and the sleepers are modelled with an anisotropic Kirchhoff plate. The solution is based on Fourier transforms in time and along the track. In the transverse direction the field in the embankment is developed in Fourier series and the fields in the ground with Fourier transforms. The resulting numerical scheme is efficient and displacements for a wide frequency spectrum can be considered. Numerical examples are given for an X2 train that operates at the site Ledsgard in Sweden. In particular, the effects of the wheel traction from the driving wheel pairs or the braking wheels (all wheels) are accounted for. The results at some instantaneous train speeds are compared to corresponding constant train speeds.

1. Introduction

With ever faster trains, excessive ground vibrations have become a problem, particularly where the ground consists of soft clays. In these materials, the shear wave velocity may be as low as 30−40 m/s, and is thus lower than some operating train speeds. A well documented case with large vibrations due to high-speed trains occurred at Ledsgard in Sweden [1–4].

Since the introduction of high-speed trains, the interest in modelling ground vibrations has increased. A common analytical approach is to represent the track with an Euler–Bernoulli beam, supported on an elastic ground. Dieterman and Metrikine [5] determine the critical speeds of a uniformly moving point load on an Euler–Bernoulli beam and give further references. Recent contributions are made by Kaynia et al. [2], Madshus and Kaynia [3] and Takemiya [4]. They model the track with a beam resting on a layered viscoelastic half-space and favourably compare the results with the measurements at Ledsgard.

An alternative to the analytical method is of course to employ FEM or some other discretization method. The advantage is the lack of restrictions on the geometries and the possibility to introduce nonlinear effects.

*Tel.: +46 31 772 1295; fax: +46 31 772 3827.
E-mail address: karand@chalmers.se.

0022-460X/$ - see front matter
doi:10.1016/j.jsv.2005.08.038

Recently, Ekevid and Wiberg [6] presented a model where the scaled boundary finite element method is used to treat the infinite domains. A disadvantage, however, is that many degrees of freedom must be adopted, which results in relatively small discretized regions. In this case, the model is 40 m long and less than that in the transverse direction (with a 107 m long train).

All models presented so far deals with constant speeds. However, de Hoop [7] models a vertical point load on an isotropic elastic half-space that is suddenly set into horizontal motion with a Heaviside unit step function and a following constant velocity. For a point load moving on an elastically supported string, a similar approach is used by Wolfert et al. [8] where a sudden increase in velocity from subcritical to supercritical is simulated with a sudden change in string density.

In this paper, the refined semi-analytical model presented by Karlström and Boström [9] is used to investigate the effects of accelerating and decelerating trains. Only the moving mass of the train is considered, i.e. influence of rail roughness, etc. is not studied. The embankment is modelled on top of the ground as a rectangular elastic region with finite width, supporting the rails and the sleepers. The rails are governed by Euler–Bernoulli's equation for flexural vibrations in the vertical and transverse directions and by the rod equation for longitudinal movement. The sleepers are introduced as an anisotropic Kirchhoff plate. The ground is modelled as a stratified half-space with viscoelastic layers.

2. Formulation of problem

To model a railway track, a rectangular embankment with the outer dimensions $2a \times d$ is situated on the surface of a layered ground, see Fig. 1. The model is defined in a cartesian coordinate system where x is the coordinate along the track, y the transverse coordinate and z the vertical coordinate. On top of the embankment, the rails are modelled as two Euler–Bernoulli beams with the width c at the positions $\pm b_R$ and the sleepers as an anisotropic Kirchhoff plate with the dimensions $2b_S \times h$. The ground consists of n layers, which are positioned with the coordinates $d_1 - d_{n-1}$, see Fig. 1. Each wheel is treated as a vertical point load acting on the rail: $F = F_0\delta(x - \int_0^t V(s)\,\mathrm{d}s)$. F_0 is the amplitude, $V(t)$ the time-dependent velocity and t the time. The wheel traction during acceleration and deceleration is also taken into account, given by the longitudinal force $F_{\mathrm{trac}} = F_{\mathrm{trac},0}\,\delta(x - \int_0^t V(s)\,\mathrm{d}s)$, where $F_{\mathrm{trac},0} = m_{\mathrm{train}}\dot{V}(t)/N_{\mathrm{wheels}}$ and m_{train} is the weight of the train and N_{wheels} is the total number of wheels transmitting the traction. A no-slip condition is assumed. The displacement components in the embankment and in the layered ground are $\mathbf{u}_j = \{u_j, v_j, w_j\}$, where u_j, v_j and w_j are the cartesian components in the x, y and z direction, respectively. The index j represents the embankment ($j = e$) and the ground layers ($j = 1, 2, \ldots, n$). The material in each layer is defined by the density ρ_j and the complex Lamé constants λ_j and μ_j. In this way, hysteretic damping (constant damping for all

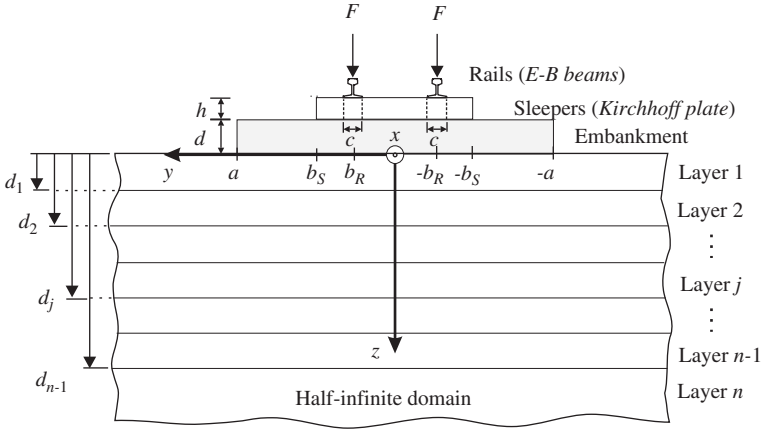

Fig. 1. A cross-section of the model showing geometrical properties and the applied wheel loads. The rails and the sleepers are introduced as boundary conditions on top of the embankment.

frequencies) is simulated. Provided the Fourier transform pair:

$$\tilde{f}(\omega) = \int_{-\infty}^{\infty} f(t)\,\mathrm{e}^{\mathrm{i}\omega t}\,\mathrm{d}t, \tag{1}$$

$$f(t) = \frac{1}{2\pi}\int_{-\infty}^{\infty} \tilde{f}(\omega)\,\mathrm{e}^{-\mathrm{i}\omega t}\,\mathrm{d}\omega, \tag{2}$$

for the time and frequency, the elastodynamic wave equation is given in the frequency domain:

$$(\lambda_j + 2\mu_j)\nabla(\nabla\cdot\tilde{\mathbf{u}}_j) - \mu_j\nabla\times(\nabla\times\tilde{\mathbf{u}}_j) = -\rho_j\,\omega^2\tilde{\mathbf{u}}_j, \tag{3}$$

where $\tilde{\mathbf{u}}_j$ is the displacement vector in layer j in the frequency domain. The wave speeds are given by $c_j^P = ((\lambda_j + 2\mu_j)/\rho_j)^{1/2}$ and $c_j^S = (\mu_j/\rho_j)^{1/2}$ for P and S waves. The traction on a plane with the normal direction $\mathbf{e}_k$ $(k = x, y, z)$ is given by

$$\tilde{\mathbf{t}}_j^{(\mathbf{e}_k)} = \lambda_j\mathbf{e}_k\nabla\cdot\tilde{\mathbf{u}}_j + 2\mu_j\partial_k\tilde{\mathbf{u}}_j + \mu_j\mathbf{e}_k\times(\nabla\times\tilde{\mathbf{u}}_j). \tag{4}$$

The gradient operator is defined as $\nabla = \{\partial_x, \partial_y, \partial_z\}$.

At each interface between two layers, i.e. at the coordinates $z = d_j$ between layer j and $j+1$, the displacement and traction vectors are continuous:

$$\tilde{\mathbf{u}}_j = \tilde{\mathbf{u}}_{j+1}, \qquad z = d_j, \tag{5}$$

$$\tilde{\mathbf{t}}_j^{(\mathbf{e}_z)} = \tilde{\mathbf{t}}_{j+1}^{(\mathbf{e}_z)}, \qquad z = d_j. \tag{6}$$

On the top surface the traction must vanish, except for the region under the embankment where the displacement and traction vectors are continuous:

$$\tilde{\mathbf{u}}_1 = \tilde{\mathbf{u}}_e, \qquad |y| < a, \quad z = 0, \tag{7}$$

$$\tilde{\mathbf{t}}_1^{(\mathbf{e}_z)} = \begin{cases} \tilde{\mathbf{t}}_e^{(\mathbf{e}_z)}, & |y| < a, \ z = 0, \\ 0, & |y| > a, \ z = 0. \end{cases} \tag{8}$$

To enable a series expansion of the displacement field in the embankment (see Section 3.2), the boundary conditions on the sides of the embankment must be designed in a special way:

$$\begin{aligned} \tilde{v}_e &= 0, \quad |y| = a, \ -d < z < 0, \\ \partial_y\tilde{u}_e &= 0, \quad |y| = a, \ -d < z < 0, \\ \partial_y\tilde{w}_e &= 0, \quad |y| = a, \ -d < z < 0, \end{aligned} \tag{9}$$

which is achieved by choosing to restrict the normal displacement component $\tilde{v}_e$ to zero and using the natural conditions on the shear stresses:

$$\begin{aligned} \tilde{v}_e &= 0, \quad |y| = a, \ -d < z < 0, \\ \tilde{\sigma}_{xye} &= 0, \quad |y| = a, \ -d < z < 0, \\ \tilde{\sigma}_{zye} &= 0, \quad |y| = a, \ -d < z < 0. \end{aligned} \tag{10}$$

Karlström and Boström [9] show that this constraint on the normal displacement gives very good approximations of the vertical displacement on top of and beside the embankment provided that the wheel loads are applied vertically. Considering that the boundary condition on the shear stress $\tilde{\sigma}_{zye} = 0$ at the sides is the natural one, this result is not unexpected. As the second shear stress component is zero, $\tilde{\sigma}_{xye} = 0$, the constraint $\tilde{v}_e = 0$ should also give a good approximation for the longitudinal displacement. It is however important that the loading is applied in the x–z plane.

By the same reasoning, the displacements in the longitudinal direction are good approximations when the traction due to acceleration is accounted for.

On top of the embankment the two rails are placed. They are characterized by the cross-sectional area A_b, the modulus of elasticity E_b, the mass density ρ_b and the moment of inertia about the y- and z-axis I_{yb} and I_{zb} (subscript b denotes beam). In the transverse direction they are governed by Euler–Bernoulli's equation and in the longitudinal direction by the rod equation.

It is recently shown by Vostroukhov and Metrikine [10] that the vertical displacement due to train passage over a track with discrete sleeper positions is almost identical to the results when the sleepers are uniformly distributed along the track. Hence the mass and stiffness from the sleepers are accounted for by introducing a transversely isotropic Kirchhoff plate [11]. The shear stiffness and the Young's modulus in the x direction should both be equal to zero if the rails are supported by sleepers. However, a slab track carries forces in the longitudinal direction via the sleepers. A transversely isotropic plate model is able to describe both situations. The plate material has a mass density ρ_s, a modulus of elasticity E_{sk} and Poisson's ratio ν_{syz} in the y–z plane and E_{sx} in the x direction and ν_{sxk} in the x–k plane, where k represents all directions perpendicular to the x direction. In the x direction the shear modulus is G_{sx} and in the isotropic y–z plane it is simply $G_{sk} = E_{sk}/2(1+\nu_{syz})$. Note that $\nu_{sxk}E_{sx} = \nu_{skx}E_{sk}$ due to symmetry of the stiffness tensor. On the free surface next to the plate, i.e. at $b_S \leqslant y < a$, the traction vanishes.

The normal and transverse components of the traction on top of the embankment thus satisfy the boundary conditions:

$$\tilde{\sigma}_{zze} = \begin{cases} -J_1\omega^2\tilde{w}_e + J_2\partial_x^4\tilde{w}_e + J_3\partial_x^2\partial_y^2\tilde{w}_e + J_4\partial_y^4\tilde{w}_e, & |y| < b_S, \ \ |y| \notin [b_R \pm c/2], \\ -I_1\omega^2\tilde{w}_e + I_2\partial_x^4\tilde{w}_e + I_3\partial_x^2\partial_y^2\tilde{w}_e + I_4\partial_y^4\tilde{w}_e - \tilde{F}/c, & |y| \in [b_R \pm c/2], \\ 0, & b_S \leqslant |y| < a, \end{cases} \tag{11}$$

$$\tilde{\sigma}_{yze} = \begin{cases} (-\rho_b A_b\omega^2\tilde{v}_e + E_b I_{zb}\partial_x^4\tilde{v}_e)/c, & |y| \in [b_R \pm c/2], \\ 0, & |y| \notin [b_R \pm c/2], \end{cases} \tag{12}$$

where

$$I_1 = J_1 + \frac{\rho_b A_b}{c}, \qquad J_1 = \rho_s h,$$

$$I_2 = J_2 + \frac{E_b I_{yb}}{c}, \qquad J_2 = \frac{h^3}{12}\left(\frac{E_{sx}^2}{E_{sx} - E_{sk}\nu_{sxk}^2}\right),$$

$$I_3 = J_3, \qquad J_3 = \frac{h^3}{6}\left(\frac{E_{sk}E_{sx}\nu_{sxk}}{E_{sx} - E_{sk}\nu_{sxk}^2} + 2G_{sx}\right),$$

$$I_4 = J_4, \qquad J_4 = \frac{h^3}{12}\left(\frac{E_{sk}E_{sx}}{E_{sx} - E_{sk}\nu_{sxk}^2}\right).$$

In the longitudinal direction the shear stress, $\tilde{\sigma}_{xze}$, accounts for both the coupling to the rails via the rod equation and the transmitted traction force during acceleration or deceleration:

$$\tilde{\sigma}_{xze} = \begin{cases} (-\rho_b A_b\omega^2\tilde{u}_e - E_b A_b\partial_x^2\tilde{u}_e)/c + \tilde{F}_{\mathrm{trac}}/c, & |y| \in [b_R \pm c/2], \\ 0, & |y| \notin [b_R \pm c/2]. \end{cases} \tag{13}$$

The boundary conditions (11)–(13) are valid for $z = -d$ and all x.

3. Exact solution

The problem formulation implies that it is convenient to apply a Fourier transform also with respect to x, where the corresponding transform variable is q. The Fourier transform pair for the space coordinate is

$$\bar{g}(q) = \int_{-\infty}^{\infty} g(x)\,\mathrm{e}^{-\mathrm{i}qx}\,\mathrm{d}x, \tag{14}$$

$$g(x) = \frac{1}{2\pi}\int_{-\infty}^{\infty} \bar{g}(q)\, \mathrm{e}^{\mathrm{i}qx}\, \mathrm{d}q. \tag{15}$$

The doubly transformed fields (with respect to t and x) are denoted by a hat.

Analytical solutions to the equations of motion (3) are obtained by decomposing the displacement field in three scalar potentials in the embankment ($j = e$) and in the ground layers ($j = 1, 2, \ldots, n$):

$$\hat{\mathbf{u}}_j = \nabla\hat{\varphi}_j + \nabla \times (\mathbf{e}_z\, \hat{\psi}_{SHj}) + \nabla \times \nabla \times (\mathbf{e}_z\, \hat{\psi}_{SVj}). \tag{16}$$

Here φ_j, ψ_{SHj} and ψ_{SVj} are potentials for longitudinal, horizontal transverse and vertical transverse waves which satisfy scalar wave equations.

3.1. Solution in the ground

In the layered ground, a Fourier transform in y makes it possible to represent the displacement fields by employing the potentials:

$$\hat{\varphi}_j = \frac{1}{2\pi}\int_{-\infty}^{\infty} (A_{jd}\mathrm{e}^{\mathrm{i}h_j^P(z-d_{j-1})} + A_{ju}\mathrm{e}^{-\mathrm{i}h_j^P(z-d_j)})\, \mathrm{e}^{\mathrm{i}py}\, \mathrm{d}p, \tag{17}$$

$$\hat{\psi}_{SHj} = \frac{1}{2\pi}\int_{-\infty}^{\infty} (B_{jd}\mathrm{e}^{\mathrm{i}h_j^S(z-d_{j-1})} + B_{ju}\mathrm{e}^{-\mathrm{i}h_j^S(z-d_j)})\, \mathrm{e}^{\mathrm{i}py}\, \mathrm{d}p, \tag{18}$$

$$\hat{\psi}_{SVj} = \frac{1}{2\pi}\int_{-\infty}^{\infty} (C_{jd}\mathrm{e}^{\mathrm{i}h_j^S(z-d_{j-1})} + C_{ju}\mathrm{e}^{-\mathrm{i}h_j^S(z-d_j)})\, \mathrm{e}^{\mathrm{i}py}\, \mathrm{d}p, \tag{19}$$

where p is the transform variable to y. The wavenumbers are $k_j^P = \omega/c_j^P$ and $k_j^S = \omega/c_j^S$ (superscript P and S denote P and S waves). Corresponding wavenumbers in the z direction are $h_j^P = (k_j^{P\,2} - q^2 - p^2)^{1/2}$ and $h_j^S = (k_j^{S\,2} - q^2 - p^2)^{1/2}$, where $\mathrm{Im}\, h_j^P \geqslant 0$ and $\mathrm{Im}\, h_j^S \geqslant 0$. With this choice of the wavenumbers, $A_{jd} = A_{jd}(p)$, $A_{ju} = A_{ju}(p)$, $B_{jd} = B_{jd}(p)$, $B_{ju} = B_{ju}(p)$, $C_{jd} = C_{jd}(p)$ and $C_{ju} = C_{ju}(p)$ are the amplitudes of the down-going (subscript d) and up-going (subscript u) P, SH and SV waves, respectively. In the last half-infinite layer ($j = n$) there are no reflected waves, i.e. $A_{nu} = 0$, $B_{nu} = 0$ and $C_{nu} = 0$, and the radiation condition with down-going or evanescent waves has been applied. The d_{j-1} and d_j in the exponents are crucial as they prevent exponential growth. With this choice, the absolute value of the exponential functions never exceeds one. When $j = 1$, by definition: $d_0 = 0$.

When the coefficients are determined, solutions (17)–(19) are used together with (16) and reverse Fourier transforms with respect to q and ω to obtain the displacement fields.

3.2. Solution in the embankment

As mentioned, the displacement field in the embankment ($j = e$) can be developed in trigonometric series and must satisfy the boundary conditions along the sides of the embankment (9). Due to the symmetric loading, the field $\mathbf{u}_e$ is symmetric about $y = 0$, which means that u_e and w_e are even and v_e is odd. Hence they are developed in Fourier cosine and Fourier sine series, with wavenumber $p_m = m\pi/a$ in the y direction. This gives the following choice for the potentials in (16):

$$\hat{\varphi}_e = \sum_{m=0}^{\infty} (D_{1m}\sin h_m^P z + E_{1m}\cos h_m^P z)\cos p_m y, \tag{20}$$

$$\hat{\psi}_{SHe} = \sum_{m=1}^{\infty} (D_{2m}\sin h_m^S z + E_{2m}\cos h_m^S z)\sin p_m y, \tag{21}$$

$$\hat{\psi}_{SVe} = \sum_{m=0}^{\infty} (E_{3m}\sin h_m^S z - D_{3m}\cos h_m^S z)\cos p_m y. \tag{22}$$

D_{nm} and E_{nm} are unknown amplitudes, where $n=1$, 2 and 3 give the amplitudes for the P, SH and SV waves, respectively. The wavenumbers are similar to those in the half-space, but with subscript e to denote the embankment: $k_e^P=\omega/c_e^P$ and $k_e^S=\omega/c_e^S$. Here the wavenumbers in the z direction are $h_m^P=(k_e^{P\,2}-q^2-p_m^2)^{1/2}$ and $h_m^S=(k_e^{S\,2}-q^2-p_m^2)^{1/2}$, where the roots are defined so that $\mathrm{Im}\,h_m^P\geqslant 0$ and $\mathrm{Im}\,h_m^S\geqslant 0$.

Similarly to the ground, the displacement field can easily be determined employing Eqs. (20)–(22) together with Eq. (16) and reverse Fourier transforms with respect to q and ω.

3.3. General solution procedure

There are two possible methods to adopt to obtain the relation between the constants in the embankment and the coefficients in the ground, one of which is the so-called Thomson–Haskell approach or transfer matrix technique [12]. The idea is to obtain a linear relation between the coefficients by recursive elimination, starting from the bottom layer. However, with increasing frequency the calculations will eventually suffer from precision problems and the algorithm becomes unstable [12]. Sheng et al. [13] modify the method to overcome the problem, whereas the global matrix approach used by e.g. Mal [12] is adopted in this model. The idea is to obtain the coefficients in the ground expressed in the constants in the embankment simultaneously for each p using the interfacial conditions (5)–(6) and the boundary condition (8). In this way all the unknowns A_{jd}, A_{ju}, B_{jd}, B_{ju}, C_{jd} and C_{ju} that depend on the continuous Fourier variable p can be expressed in D_{nm} and E_{nm} (which do not depend on p).

Employing an inverse Fourier series with respect to y over the width of the embankment ($-a<y<a$) of the boundary condition (7) together with similar inverse Fourier series of the boundary conditions on top of the embankment (11)–(13), the remaining unknowns D_{nm} and E_{nm} are solved. The calculations are outlined in the paper by Karlström and Boström [9].

3.4. The acceleration

The time-dependent velocity $V(t)$ is crucial in the Fourier transform of the force in Eq. (11):

$$\hat{F}=F_0\int_{-\infty}^{\infty}\int_{-\infty}^{\infty}\delta\left(x-\int_0^t V(s)\,\mathrm{d}s\right)\mathrm{e}^{\mathrm{i}(\omega t-qx)}\,\mathrm{d}x\,\mathrm{d}t \tag{23}$$

and similar for the traction force in Eq. (13). However, if the train travels with the constant velocity V_0 the expression is simplified:

$$\hat{F}=F_0\int_{-\infty}^{\infty}\int_{-\infty}^{\infty}\delta(x-V_0t)\,\mathrm{e}^{\mathrm{i}(\omega t-qx)}\,\mathrm{d}x\,\mathrm{d}t=F_0\frac{2\pi}{|V_0|}\delta\left(\frac{\omega}{V_0}-q\right). \tag{24}$$

This enables very fast computations, since the inverse Fourier transform with respect to q becomes trivial, i.e. $q=\omega/V_0$ (typically around 1 min for a $200\times 200\,\mathrm{m}^2$ domain with a frequency content of $0<f<3\,\mathrm{Hz}$).

The simulation for an accelerating or decelerating train takes much longer time than when a constant train speed is considered. This is due to the extra integral over q in the reverse Fourier transform. The x integral in Eq. (23) is trivial to carry out due to the Dirac delta function. But because of this the exponential function becomes hard to integrate analytically over t. However, with a linear train velocity $V(t)$ and a careful choice of the time history, see Fig. 2, Eq. (23) can be simplified:

$$\hat{F}=F_0\frac{2\pi}{|V_0|}\delta\left(\frac{\omega}{V_0}-q\right)+F_0\int_0^{t_{\mathrm{end}}}\left(\mathrm{e}^{\mathrm{i}(\omega t-q\int_0^t V(s)\,\mathrm{d}s)}-\mathrm{e}^{\mathrm{i}t(\omega-qV_0)}\right)\mathrm{d}t. \tag{25}$$

As the average velocity within $t=0$ and t_{end} is V_0 and the constant velocities before and after is V_0, the transformed force is decomposed in the constant velocity contribution given by Eq. (24) and a time-dependent part which involves the Fresnel integrals $C(x)$ and $S(x)$ defined by

$$C(x)=\int_0^x\cos\frac{\pi t^2}{2}\,\mathrm{d}t, \tag{26}$$

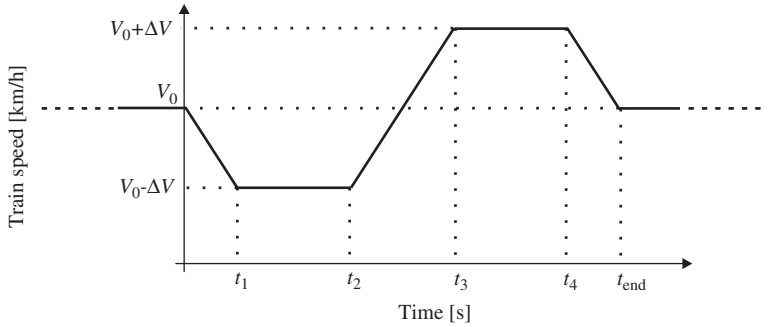

Fig. 2. The time history of the train speed used during deceleration and acceleration.

$$S(x) = \int_0^x \sin\frac{\pi t^2}{2}\,\mathrm{d}t, \tag{27}$$

which has to be evaluated by means of well-known series expansions.

4. Numerical examples

Madshus and Kaynia [3] use the program "VibTrain" described in [2] to predict the ground vibrations observed at the site Ledsgard. They represent the track by a beam with finite elements resting on a layered ground. A similar approach is taken by Takemiya [4], where the track is represented by an Euler–Bernoulli beam. When the train travels with subcritical speeds, the strain levels in the ground are moderate, but as the train speed is close to or higher than the Rayleigh wave speed for the ground, the strains increase drastically. Due to nonlinearities in the soils, the material parameters become highly dependent on the velocity, therefore mainly two train speeds have been investigated: 70 km/h (subcritical) and 200 km/h (supercritical). The ground is modelled with five layers ($n = 5$) and the soil parameters adopted for the present model are tabulated in Table 1, based on the comprehensive measurements performed by the Swedish National Rail Administration BANVERKET and used by Kaynia et al. [2], Madshus and Kaynia [3] and Takemiya [4].

Both the geometrical and material properties for the embankment are somewhat uncertain. For the beam used in "VibTrain", Kaynia et al. [2] use the bending stiffness $EI = 200\,\mathrm{MN\,m^2}$ at low train speeds and $EI = 80\,\mathrm{MN\,m^2}$ at high speeds, and the mass density is taken as 10 800 kg/m. In the paper presented by Madshus and Kaynia [3], a cross-section of a part of the track structure at Ledsgard (consisting of three tracks) is outlined. Assuming that Madshus and Kaynia [3] use a symmetric embankment with the dimensions $1.4 \times 8.0\,\mathrm{m^2}$ to obtain the bending stiffness for their beams, the modulus of elasticity for the embankment is obtained from the given bending stiffness at low and high train speeds (excluding the bending stiffness for the rails).

By experience, see Ref. [9], the embankment defined by the cross-sectional area $0.5 \times 8.0\,\mathrm{m^2}$ together with the mass density $\rho_e = 1800\,\mathrm{kg/m^3}$ [3] and the Poisson ratio $\nu_e = 0.3$ gives results that agree very well with the measurements at both 70 and 200 km/h at Ledsgard.

On top of the embankment the rails are placed. They are standard UIC60 rails with cross-sectional area $A_b = 76.87\,\mathrm{cm^2}$, modulus of elasticity $E_b = 210\,\mathrm{GPa}$, density $\rho_b = 7850\,\mathrm{kg/m^3}$ and moment of inertia about the y- and z-axis $I_{yb} = 3055\,\mathrm{cm^4}$ and $I_{zb} = 516.4\,\mathrm{cm^4}$ [14]. The base that is in contact with the embankment is $c = 15\,\mathrm{cm}$ and the span of the rails is $2\,b_R = 1.5\,\mathrm{m}$, see Fig. 1.

A standard mono-block sleeper coded NS 90 [14] has the outer dimensions $2520 \times 300 \times 233\,\mathrm{mm^3}$ (length × width × height) and are distributed with the regular intervals 0.67 m [3]. In this model, the distributed mono-block sleepers are modelled with the transversely isotropic (in the y–z plane) Kirchhoff plate, which has the width 2520 mm, the height 233 mm and an infinite length along the track. The weight of one sleeper is within 200–300 kg, why the average of 250 kg gives the mass density of the plate $\rho_s = 635\,\mathrm{kg/m^3}$. With the modulus of elasticity $E_s = 38\,450\,\mathrm{MPa}$ for one sleeper [15] the stiffness in the y–z plane becomes $E_{sk} = 38\,450\,\mathrm{MPa}$. As the sleepers are supported directly on the gravel on the embankment, the stiffness in the x direction is chosen to be

Table 1
Soil parameters from the test site Ledsgard [3,4], used in the simulations for low train speeds ($V_0 = 70$ km/h) and high train speeds ($V_0 = 200$ km/h)

Soil layer	Thickness (m)	Mass density, ρ_j (kg/m^3)	c_s (m/s)		c_p (m/s)		Damping ratio, δ_j	
			$V_0 = 70$	$V_0 = 200$	$V_0 = 70$	$V_0 = 200$	$V_0 = 70$	$V_0 = 200$
Surface crust ($j = 1$)	1.1	1500	72	65	500	340	0.04	0.063
Organic clay ($j = 2$)	3.0	1260	41	33	500	360	0.02	0.058
Marine clay ($j = 3$)	4.5	1475	65	60	1500	1500	0.05	0.098
Marine clay ($j = 4$)	6.0	1475	87	85	1500	1500	0.05	0.064
Marine clay ($j = 5$)	∞	1475	100	100	1500	1500	0.05	0.060

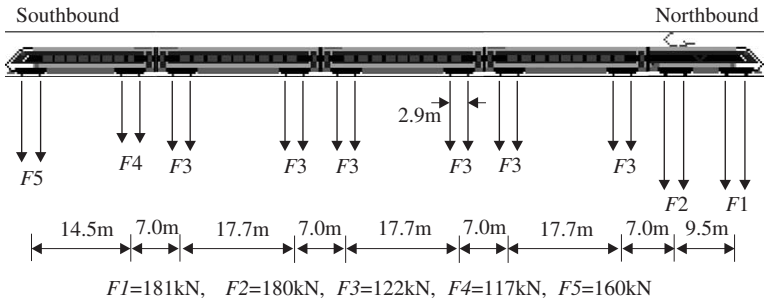

Fig. 3. The X2 train configuration that is used in the model, showing the geometrical properties and the axle-loads F1–F5.

zero, $E_{sx} = 0$ MPa, as well as the shear modulus, $G_{sx} = 0$ MPa. The Poisson's ratio is assumed to be $\nu_{syz} = \nu_{sxk} = 0.2$ with some uncertainty, but experience shows that this does not affect the results (k is any direction perpendicular to the x direction).

The axle-load is introduced via Eqs. (11), (23) and (24) and in the model it is superimposed to yield an X2 train with five cars, one of which is the engine, see Fig. 3. It has the same configuration as the train that operated along the west coast line during the measurements at Ledsgard [1–4]. When the train accelerates it is assumed that the two wheel pairs denoted with $F2$ are transmitting the driving traction force and when it decelerates all wheels are assumed to brake simultaneously.

4.1. The instantaneous speed, 70 km/h

The speed history of the X2 train in Fig. 2 is chosen to simulate an acceleration/deceleration of $|\dot{V}(t)| \approx 2.2\,\mathrm{m/s^2}$. This is obtained by choosing $V_0 = 90$ km/h, $\Delta V = 40$ km/h, $t_1 = 5$ s, $t_2 = 20$ s, $t_3 = 30$ s, $t_4 = 45$ s and $t_5 = 50$ s. Hence, the velocity, 70 km/h, that is of interest occurs after 2.5 s during the deceleration and after 22.5 s during the acceleration.

In Fig. 4, the frequency responses (at the right) are seen for the vertical displacements on top of the embankment at $y = 0$ where the middle of an X2 train passes with the instantaneous velocity of 70 km/h during deceleration (dotted curve) and during acceleration (dashed curve). In addition, the response at the constant velocity of 70 km/h is shown (solid line). The corresponding time domain results are plotted relative to the front of the train at the left. Here it can be stated that when the train brakes with all wheels, the vertical displacement is almost identical to the case when the train travels with constant speed. This is also seen in the frequency spectrum, where the levels are overall the same as for the constant train speed. However, the interference pattern is shifted towards lower frequencies, at least for frequencies less than 2 Hz.

The similar time domain result is obtained when the train accelerates, but with somewhat reduced displacement levels under the last half of the train and on the tail left behind the train. The levels of the frequency response are in general the same as for the other cases, but with a higher contribution at about 0.8 Hz.

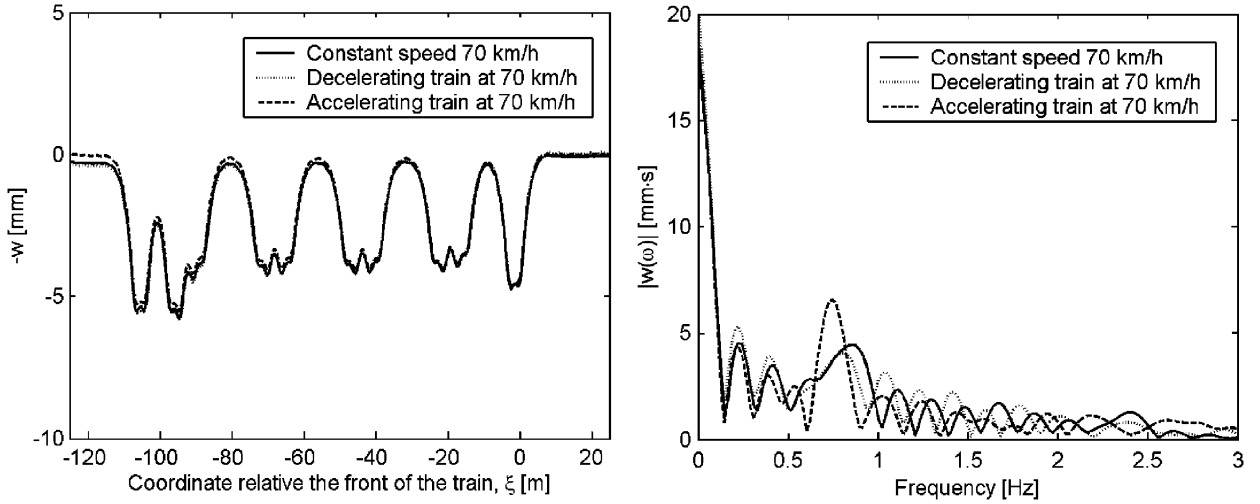

Fig. 4. Vertical response at the instantaneous speed of 70 km/h for a train at constant speed (solid curve), at deceleration (dotted curve) and at acceleration (dashed curve). The time domain result is seen in the left figure and the frequency spectra in the right at a position under the middle of the train at $y = 0$ and $z = -d$.

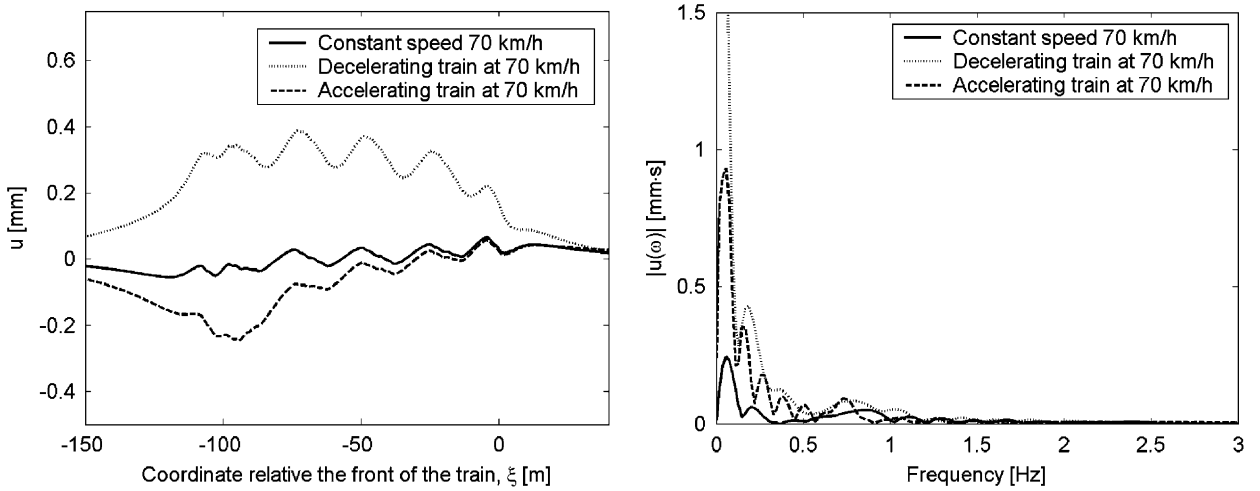

Fig. 5. Longitudinal response at the instantaneous speed of 70 km/h for a train at constant speed (solid curve), at deceleration (dotted curve) and at acceleration (dashed curve). The time domain result is seen in the left figure and the frequency spectra in the right at a position under the middle of the train at $y = 0$ and $z = -d$.

Similarly to the vertical response, the longitudinal (in the x direction) frequency spectra and physical displacement components u_e relative the front of the train are shown in Fig. 5. As expected, the displacements under the wheels are positive during the retardation and negative during the acceleration. In particular, the acceleration causes a large shear at the wheel contacts under the driving wheel pairs. In the frequency response it is seen that the longitudinal displacements for the three cases are dominated by frequencies less than 1 Hz and that the static contribution during deceleration is in particular high (about 4.5 mm s at 0 Hz).

4.2. The instantaneous speed, 200 km/h

The displacements for the high-speed train has been investigated around 200 km/h in a similar way as for the low-speed train. The same amount of acceleration is adopted, which means that the average velocity has to be changed to $V_0 = 220$ km/h.

In Fig. 6, the vertical displacement is seen at a position under the middle of the train and at $y = 0$ and $z = -d$. In the left figure, the time domain results are shown for the constant train speed (solid curve), the decelerating train speed (dotted curve) and the accelerating train speed (dashed curve). At the right, the corresponding frequency contents are shown. As for the low train speed, the time domain displacements agree relatively well during the deceleration and the acceleration compared to the constant speed. This is also seen in the frequency response plot. The same shift as for the low train speed is however not seen at higher train speeds.

Similarly in Fig. 7, the longitudinal displacements at 200 km/h are seen under the middle of the train at constant velocity (solid curve), during deceleration (dotted curve) and during acceleration (dashed curve). To

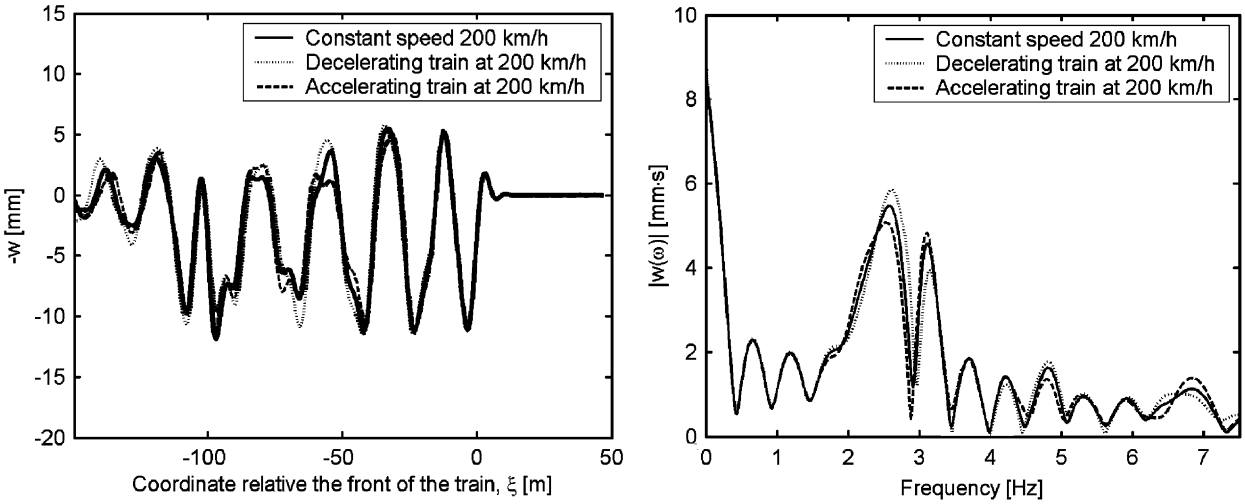

Fig. 6. Vertical response at the instantaneous speed of 200 km/h for a train at constant speed (solid curve), at deceleration (dotted curve) and at acceleration (dashed curve). The time domain result is seen in the left figure and the frequency spectra in the right at a position under the middle of the train at $y = 0$ and $z = -d$.

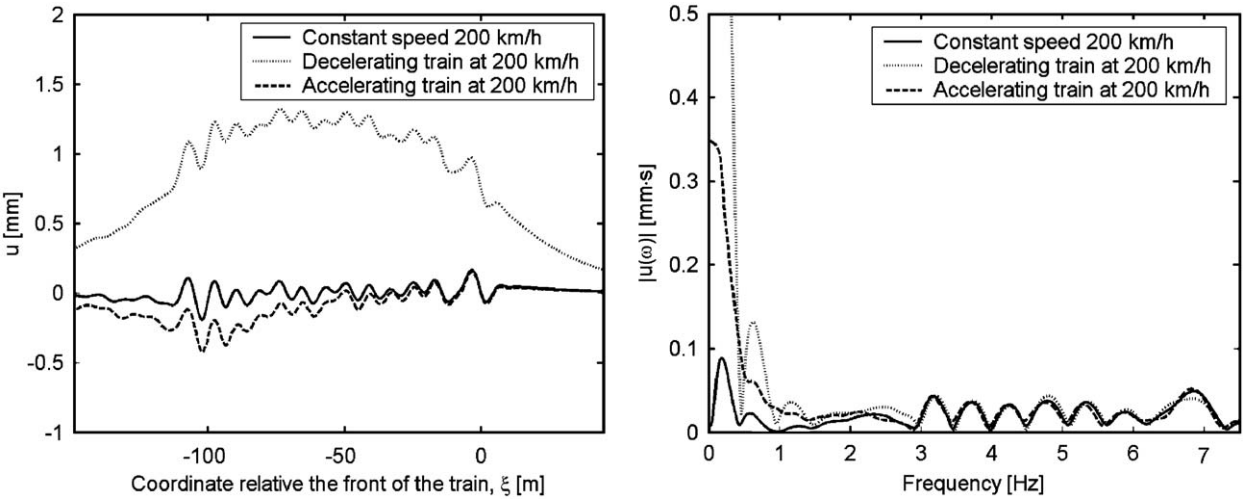

Fig. 7. Longitudinal response at the instantaneous speed of 200 km/h for a train at constant speed (solid curve), at deceleration (dotted curve) and at acceleration (dashed curve). The time domain result is seen in the left figure and the frequency spectra in the right at a position under the middle of the train at $y = 0$ and $z = -d$.

the left, the time domain displacements are shown and to the right the frequency spectra. As for the train at 70 km/h, the deceleration gives large positive displacements at the wheel contacts and during the acceleration the two driving wheel pairs causes the ground to deflect in the negative direction. Compared to the case at 70 km/h, the shear during deceleration is increased with more than a factor three, whereas the acceleration gives the similar amplitudes. The frequency response consists of large static contributions, mainly for the decelerating train (about 3.5 mm s at 0 Hz), but contrary to the low train speed also components of higher frequencies (up to 7.5 Hz) are significant. The differences in the time domain displacements between the three cases are however only due to differences for frequencies lower than 3 Hz.

5. Concluding remarks

In this paper, the ground vibrations from an accelerating X2 train is investigated with the presented semi-analytical approach. Especially, the effects of the wheel traction is accounted for. During deceleration, all wheels are assumed to act simultaneously, while during acceleration only the traction from the two driving wheel pairs are added. Simulated displacements on top of the embankment are investigated at the instantaneous train speeds of 70 and 200 km/h. In addition, the results for the corresponding constant train speeds are included.

At both 70 and 200 km/h, the differences in vertical displacement between a train at constant velocity and both an accelerating and a decelerating train are relatively small. In the longitudinal direction, however, there are large differences. During deceleration, the wheel traction causes a large positive shear of the surface material in the embankment. The opposite occurs during acceleration, where in particular the driving wheel pairs cause a large shear of the surface material under their wheel contacts. The behaviour is typical at both 70 and 200 km/h and the deflections are dominated by low frequencies.

Acknowledgements

This work is part of the activities of the Center of Excellence CHARMEC (CHAlmers Railway MEChanics, www.charmec.chalmers.se). The project was supervised by Professor Anders Boström at the Department of Applied Mechanics at Chalmers.

References

[1] Banverket, High speed lines on soft ground: evaluation and analyses of measurements from the West Coast line, Swedish National Rail Administration, Borlänge, Sweden, 1999.
[2] A.M. Kaynia, C. Madshus, P. Zackrisson, Ground vibration from high-speed trains: prediction and countermeasure, *Journal of Geotechnical and Geoenvironmental Engineering* 126 (6) (2000) 531–537.
[3] C. Madshus, A.M. Kaynia, High-speed railway lines on soft ground: dynamic behaviour at critical train speed, *Journal of Sound and Vibration* 231 (3) (2000) 689–701.
[4] H. Takemiya, Simulation of track-ground vibrations due to a high-speed train: the case of X2000 at Ledsgard, *Journal of Sound and Vibration* 261 (3) (2003) 503–526.
[5] H.A. Dieterman, A. Metrikine, The equivalent stiffness of a half-space interacting with a beam, Critical velocities of a moving load along the beam, *European Journal of Mechanics—A/Solids* 15 (1) (1996) 67–90.
[6] T. Ekevid, N.-E. Wiberg, Wave propagation related to high-speed train: a scaled boundary FE-approach for unbounded domains, *Computer Methods in Applied Mechanics and Engineering* 191 (36) (2002) 3947–3964.
[7] A.T. de Hoop, The moving-load problem in soil dynamics—the vertical displacement approximation, *Wave Motion* 36 (4) (2002) 335–346.
[8] A.R.M. Wolfert, H.A. Dieterman, A.V. Metrikine, Passing through the "elastic wave barrier" by a load moving along a waveguide, *Journal of Sound and Vibration* 203 (4) (1997) 597–606.
[9] A. Karlström, A. Boström, An analytical model for train induced ground vibrations from railways, *Journal of Sound and Vibration*, in press, doi:10.1016/j.jsv.2005.07.041.
[10] A.V. Vostroukhov, A.V. Metrikine, Periodically supported beam on a visco-elastic layer as a model for dynamic analysis of a high-speed railway track, *International Journal of Solids and Structures* 40 (21) (2003) 5723–5752.
[11] S.A. Ambartsumyan, *Theory of Anisotropic Plates*, Vol. II, Technomic Publication, Stamford, USA, 1970.
[12] A.K. Mal, Wave propagation in layered composite laminates under periodic surface loads, *Wave Motion* 10 (3) (1988) 257–266.

[13] X. Sheng, C.J.C. Jones, M. Petyt, Ground vibration generated by a load moving along a railway track, *Journal of Sound and Vibration* 228 (1) (1999) 129–156.
[14] C. Esveld, *Modern Railway Track*, MRT-Productions, Duisburg, West Germany, 1989.
[15] G. Kumaran, D. Menon, K.K. Nair, Dynamic studies of railtrack sleepers in a track structure system, *Journal of Sound and Vibration* 268 (3) (2003) 485–501.